CrystEngComm

ROYAL SOCIETY OF CHEMISTRY

The controlled transition-metal doping of SnO₂ nanoparticles with tunable luminescence

M. A. Peche-Herrero,[a] D. Maestre,*[b] J. Ramírez-Castellanos,[a] A. Cremades,[b] J. Piqueras[b] and J. M. González-Calbet[a]

SnO₂ nanoparticles doped with transition metals (V, Cr, Mn) have been synthesized by both the hydrothermal method (HDT) in a basic media and the liquid mixed method (LQM) based on the Pechini method. Nanocrystalline particles obtained *via* a liquid mixed technique show a well-defined chemical composition and an average size of 6 nm, with a high degree of both crystallinity and chemical homogeneity. Nanoparticles prepared *via* a hydrothermal method exhibit a high dispersion in size as well as agglomeration effects. As the LQM demonstrates advantages with respect to the HDT, a more detailed investigation has been carried out on the SnO₂ nanoparticles doped with V, Cr and Mn grown by this method. The microstructure of the materials was elucidated by means of X-ray Diffraction (XRD), Selected-Area Electron Diffraction (SAED), and High-Resolution Transmission Electron Microscopy (HRTEM). Luminescence from undoped and doped SnO₂ nanoparticles was characterized by cathodoluminescence (CL). The luminescence studies demonstrate a strong dependence of CL signals with transition metal doping, thus inducing red, green or orange emissions when doping with Cr, V or Mn respectively.

Introduction

SnO₂ cassiterite is a wide-band gap n-type semiconductor (E_g = 3.6 eV at 300 K) with excellent electrical, optical and electrochemical properties[1,2] which make it suitable for numerous technological applications. During previous years the capabilities of this material have been exploited in diverse fields such as gas sensing,[3–5] solar cells,[6] catalysis,[7] optoelectronics,[8,9] or as a diluted magnetic semiconductor (DMSO),[10,11] in all of which low dimensional structures play a key role. Facing these applications, new challenging performances of SnO₂ have been recently developed, such as SnO₂/graphene nanocomposites and SnO₂ nanoparticles as promising materials for high capacity Li-ion battery anodes,[12,13] or SnO₂-based spintronic devices,[14] among others. Hence, in order to optimize these potential applications and to extend the applicability of this material, it is important to improve the synthesis methods that are able to control with high accuracy the size, morphology and composition of the SnO₂ nanostructures. In particular the achievement of a controlled doping of nanostructures, with a high concentration of doping atoms

and cationic ordering, is a difficult issue in which great efforts are invested, as it is of the utmost importance for the control of the performance of SnO₂ based electronic and optoelectronic devices.

Several chemical methods have been developed so far in order to obtain SnO₂ nanoparticles such as hydrothermal methods,[15,16] sol–gel,[17–21] co-precipitation,[5,10,22] chemical vapor deposition (CVD),[4] mechanical synthesis,[11,23] laser pyrolysis,[24] and thermal evaporation.[25] In this paper we applied and evaluated the advantages and drawbacks of two soft chemistry methods in order to obtain optimized nano-sized materials. In this sense, both the hydrothermal method (HDT) and the less extended liquid mix method (LQM)[26] have been used and evaluated in this work for the synthesis of doped nanoparticles. The HDT was chosen as a comparative soft chemical route because it is a proven method to obtain nanoparticles due to the special conditions that can be reached at low temperatures, which permits the obtention of smaller particles.[15] It has been only recently that the LQM has been employed for the synthesis of doped nanoparticles, as this synthetic pathway developed for the preparation of mixed oxides allows the production of reproducible quantities with a precise homogeneity in both composition and particle size, as demonstrated in this work. In this case the basic concept is to stabilize an aqueous solution of the desired cations with citric acid, or other hydroxy–carboxylic acids. The high-complexing potential of these acids avoids the precipitation of

[a] *Departamento de Química Inorgánica I, Facultad de Ciencias Químicas, Universidad Complutense de Madrid, 28040 Madrid, Spain*
[b] *Departamento de Física de Materiales, Facultad de Ciencias Físicas, Universidad Complutense de Madrid, 28040 Madrid, Spain. E-mail: davidmaestre@fis.ucm.es*

the dissolved metals when the solvent is evaporated, which maintains this homogeneity in the solid state. In this way, not only a precise control of the cationic concentration is possible, but also the diffusion process is enormously favored by means of the liquid solution, as compared to other classical methods. In particular, to the best of our knowledge, the LQM has not been previously used for the synthesis of V, Cr and Mn doped SnO_2 nanoparticles, therefore these results will provide valuable knowledge both for applications and fundamental research. In addition, despite of the fact that in this work only transition metals (V, Cr, Mn) have been used as dopants, the here-described synthesis methods can be also extended to the growth of some other doped materials. In particular, transition metal (V, Cr, Mn) doped semiconductor nanoparticles, such as those investigated in this work, are emerging as promising candidates for spintronic and opto-electronic applications, hence further research should be invested on the understanding of the effects promoted by a controlled size and cationic composition on their physical–chemical properties. The structure of the defects, the effectiveness of the dopant incorporation, the achievement of a high-controlled cationic composition, the structural stability, the interplay of the native defects with the dopants, the influence of the dopants in both the growth process and the modulation of the electrical and optical properties, or the relationship between the electronic structure of the doped SnO_2 nanoparticles and their functional properties, are crucial aspects which need to be deeply investigated in order to integrate doped nanoparticles into advanced devices. In this sense, the cathodoluminescence (CL) technique is an useful tool to further analyze the structure of the defects and the effects of the doping on SnO_2, as metal ions usually introduce localized states in the band gap as well as defect related levels, mainly associated with oxygen vacancies or Sn interstitials, which influence the luminescence properties of the nanostructures.

Following these ideas, we discuss the synthesis of the undoped SnO_2 and $Sn_{1-x}M_xO_2$ (M = V, Cr and Mn, $0 \leq x \leq 0.15$) nanoparticles through two different preparation methods, HDT and LQM. The materials were characterized by X-Ray Diffraction (XRD), X-ray Energy Dispersive Spectroscopy (EDS), High-Resolution Transmission Electron Microscopy (HRTEM) and Cathodoluminescence (CL) in a Scanning Electron Microscope (SEM).

Materials and methods

Sample preparation

The undoped SnO_2 and $Sn_{1-x}M_xO_2$ (x = 0, 0.05, 0.1, 0.15; M = V, Cr, Mn) samples were prepared via two different wet chemical routes in order to obtain nanopowders with a controlled particle size, morphology and composition. In both cases, stoichiometric amounts of $Sn(CH_3COO)_2$ (Aldrich 99.99%), $SnCl_4 \cdot 5H_2O$ (Aldrich 99.99%), NH_4VO_5 (Aldrich 99%), $Cr(NO_3)_3 \cdot 9H_2O$ (Aldrich 99.99%), $MnCO_3$ (Aldrich 99.9%), NaOH, ethanol, citric acid ($C_6O_7H_8$) and ethylene glycol ($C_2O_2H_6$) (Aldrich) were used as starting materials.

In the hydrothermal method (HDT) an ethanol solution of sodium hydroxide was added dropwise to a 0.15 M aqueous solution of tin chloride and the corresponding dopant precursor, until pH = 12. The obtained solution was introduced into a Teflon lined non-stirred pressure vessel, and it was then heated in an oven for 12 hours at 180 °C. Afterwards, the oven was cooled down to room temperature and the products were rinsed with water and ethanol, and then finally dried at 60 °C.

In the polymeric precursor method, also known as the "liquid mix method" (LQM), a 0.35 M solution of citric acid in deionized water, containing stoichiometric amounts of the Sn precursor and the selected dopant precursor, was heated with continuous stirring. Hydrochloric acid was added as a catalyst to obtain a clear solution. Subsequently, ethylene glycol was added (3% v/v) to a mixture of the above-mentioned solutions in order to start the gelation as it reacted with the citric solution. This avoids the formation of partial segregations, which could modify the homogeneity of the solution. The evaporation of the solution gives a vitreous intermediate polymer, which contains all of the cations in the desired stoichiometric amounts. Finally, the resin was calcined, which resulted in a fine powder containing doped tin oxide nanoparticles. The powders were treated at 350 °C for 30 hours in order to completely remove all organic residues, and then at 450 °C overnight in order to improve the crystallinity. A schematic representation of both synthesis methods is shown in Scheme 1.

A carbon-content analysis was performed on a Perkin Elmer 2400 CHN analyzer, with ± 0.01% error. This elemental carbon analysis showed a carbon content lower than that of the quantification limit of the equipment, so that carbon impurities could be discarded.

X ray diffraction characterization

Samples were studied by X-Ray diffraction (XRD) using a Siemens D5000 diffractometer. The data were collected at 2θ
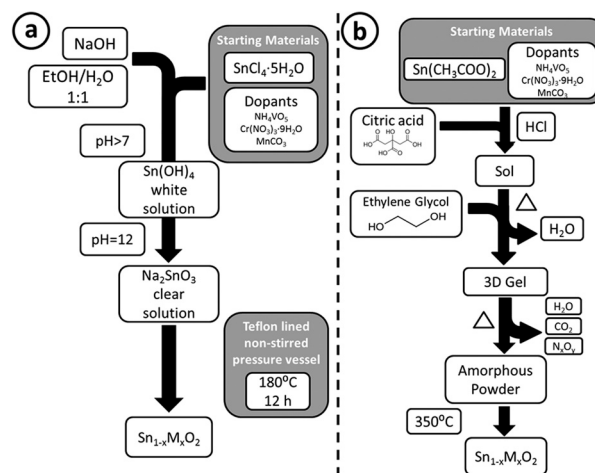
Scheme 1 The synthesis diagram of (a) the HDT and (b) LQM.

between 10° and 70°, with a step size of 0.04° and a collection time of 1 s per step. The working radiation was Cu(K$_\alpha$) (λ = 1.5418 Å).

For the cell parameter measurements and Rietveld refinement analysis, the XRD patterns were taken in a Panalytical X'Pert Pro Alpha1 instrument, equipped with a primary fast X'Celerator detector operating at 45 kV and 40 mA, and fitted with a primary curved Ge 111 monochromator in order to get Cu K$_{\alpha1}$ radiation (λ = 1.5406 Å).

Selected area electron diffraction, high resolution electron microscopy and energy-dispersive X-ray spectroscopy

Selected Area Electron Diffraction (SAED) and High Resolution Electron Microscopy (HRTEM) were performed in a JEOL 300 FEG electron microscope, fitted with a GATAN double tilt goniometer stage (±22°, ±22°). The local composition was analyzed by energy-dispersive X-ray spectroscopy (EDS) using an Oxford INCA analyzer system attached to the above-mentioned microscope. Further HRTEM image analysis was performed with Digital Micrograph software, and image calculations were performed by means of a MacTempas software program.

Cathodoluminescence analysis

Cathodoluminescence measurements were carried out in a Hitachi S2500 SEM at different temperatures ranging from 80 to 300 K, with a beam energy of 18 keV. A Hamamatsu R928 photomultiplier and a Hamamatsu PMA-11 charge-coupled device camera were utilized for the analysis of the CL signal.

Results and discussion

Structural characterization

The XRD results have been systematically analyzed as a function of the type of dopant (V, Cr, Mn), as well as the cationic concentrations in which the dopants have been incorporated (5%, 10%, 15%). The XRD patterns show that all of the samples, either synthesized by the HDT or the LQM, exhibit a cassiterite structure (rutile-type, tetragonal unit cell, S.G. $P4_2/mnm$, and lattice parameters of $a = b = 4.74$ Å and $c = 3.19$ Å), as observed in the refined XRD data of the undoped and V, Cr and Mn doped SnO$_2$ samples obtained by the LQM, which are shown in Fig. 1.

Regarding the doped samples, the substitution of Sn for V, Cr and Mn, induced a slight decrease in the lattice parameters of the LQM doped phases as compared to that of the pure SnO$_2$. This parameter decrease is due to the fact that the ionic radii of the incorporated dopants were smaller than the Sn radius.[27] This effect becomes more noticeable as the dopant cationic concentration is increased up to 15%, which shows that the rutile structure has adjusted to a variation in the substituted atom radius. Unlike the LQM samples, in all of the HDT doped samples the segregation of a second phase of the dopant oxide occasionally occurs, as detected by XRD.

The average grain sizes of the nanoparticles prepared by both techniques were calculated using the Scherrer formula,
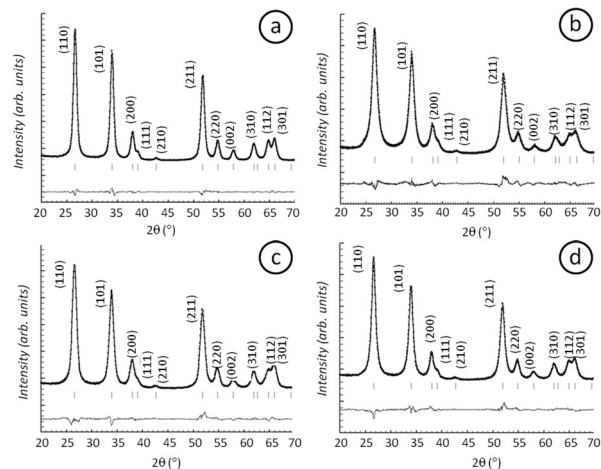

Fig. 1 The XRD patterns of the (a) undoped SnO$_2$ and (b) V, (c) Cr and (d) Mn doped SnO$_2$ synthesized by the LQM.

$D = k\lambda/B \cos \theta$, where θ is the peak position, λ is the x-ray wavelength and B is the Full Weight Half Maximum (FWHM) of the diffraction maxima.

After the Rietveld analysis of the monochromatic X-ray data, values around 8.7 nm have been obtained for the undoped SnO$_2$ nanoparticles synthesized by the LQM. The doped nanoparticles show reduced dimensions compared to the undoped ones, as summarized in Table 1, where the averaged sizes corresponding to samples doped with a 15% cationic fraction of V, Cr and Mn are shown. The estimated size for the Cr and Mn doped SnO$_2$ nanoparticles is around 6.5 nm. In the case of the vanadium-doped nanoparticles the estimated sizes were slightly smaller. X-ray data obtained from this chemical substitution study showed that the metal doping favors the growth of smaller nanoparticles. This shows that the role played by the doping element in the LQM can be discussed as an inhibitor of the crystal growth.[28]

The undoped hydrothermal samples show a higher average size of around 16 nm. The TEM techniques prove that this XRD-estimated value is an average, and that the synthesized nanoparticles obtained by this method exhibit a high degree of agglomeration, a distribution of sizes wider than the LQM case and the presence of elongated irregular nanocrystals, which can be explained in pH terms, which markedly alter the particle growth rate. During the hydrolysis process of the Sn precursor in the HDT, Sn–OH links were formed, thus producing Sn(OH)$_4$ which transforms into an amorphous phase and after hydrothermal treatment at 180 °C for 15 hours, finally

Table 1 The cell parameters, average size (D) and wellness factors of the Rietveld analysis corresponding to the undoped and doped SnO$_2$ nanoparticles fabricated by the LQM

	a (Å)	c (Å)	D (Å)	R_p	R_{wp}	R_{exp}	x^2
SnO$_2$	4.73(5)	3.18(5)	86.92 ± 0.05	3.04	4.03	4.00	1.51
Sn$_{0.85}$V$_{0.15}$O$_2$	4.72(2)	3.18(2)	51.13 ± 0.04	4.83	6.12	3.54	2.99
Sn$_{0.85}$Cr$_{0.15}$O$_2$	4.73(4)	3.18(4)	65.41 ± 0.02	4.48	5.78	3.44	2.83
Sn$_{0.85}$Mn$_{0.15}$O$_2$	4.72(5)	3.17(5)	65.26 ± 0.02	3.75	4.71	3.41	1.91

forms SnO_2. The presence of the elongated nanocrystals is an indication of the fact that particle growth occurs due to grain rotation induced by a grain coalescence mechanism.[29,30] Some reports[31] indicate that the presence of a high OH^- concentration was found to enhance the agglomeration of the nanocrystals, which favors the growth of elongated nanocrystals since the formation of the SnO_2 nanoparticles occurs *via* a meta-stable phase $Sn(OH)_4$, which does not directly transform into SnO_2, but into an amorphous phase, and then grows. Moreover, it is well known that nucleation at the interfaces (*i.e.* heterogeneous nucleation) dominates other nucleation processes. The boundaries of the amorphous solid particles offer such interfaces and therefore it is reasonable to assume that the nucleation of SnO_2 is a heterogeneous nucleation process.

A low magnification TEM micrograph of the HDT samples confirms the high degree of agglomeration and heterogeneous sizes, as nanoparticles from 5 to some tens of nanometers can be observed in Fig. 2a. A small amount of crystals with a regular shape was also found in the reaction products. The interatomic distances of 3.08 and 7.43 Å are measured in the HRTEM image of this material in Fig. 2b. The upper inset (Fig. 2c) shows the corresponding FFT pattern of the highlighted nanoparticle, indexed along the [1$\bar{1}$1] zone axis of the rutile structure.

On the contrary, the nanoparticles obtained by the LQM show high homogeneity in size (below 10 nm) and shape, as shown in Fig. 3a, which is in good agreement with the results of the Rietveld analysis (Table 1). The high control of the dimensions of the nanoparticles fabricated *via* the LQM, as well as the associated size homogeneity, together with the fact that the dopant oxide segregation observed for the HDT samples is avoided in this case, make the LQM more appropriate for the obtention of doped nanoparticles. Therefore, a detailed TEM study of the transition metal (V, Cr, Mn) doped SnO_2 nanoparticles synthesized by the LQM has been performed. In these samples, a controlled composition of 5, 10 or 15% cationic composition has been successfully achieved, and phases with a tailored composition were stabilized. Fig. 3b shows the HRTEM image of an isolated
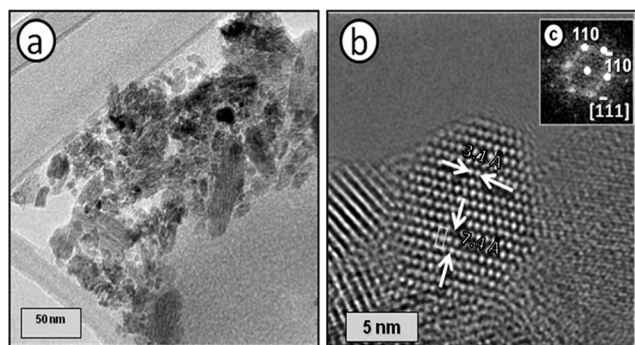

Fig. 3 (a) Low magnification HRTEM image of undoped SnO_2, (b) HRTEM image of a $Sn_{0.85}Mn_{0.15}O_2$ isolated nanoparticle prepared by the liquid mix method (LQM), the reticular parameters and unit cell of the rutile basal plane can be seen. (c) FFT pattern along the [001] axis of the rutile structure.

$Sn_{0.85}Mn_{0.15}O_2$ nanoparticle, which is representative from the Mn doped nanoparticles. The interplanar distances of 0.48 nm can be measured along both perpendicular directions, corresponding to the unit cell of the material, which is marked by a square. The FFT pattern (Fig. 3c) can be indexed on the basis of the rutile crystal structure along the [001] zone axis.

Fig. 4a shows the HRTEM image of the $Sn_{0.85}Cr_{0.15}O_2$ nanoparticles, as an example of the Cr doped nanoparticles. The corresponding FFT pattern along the [011] zone axis can be observed in Fig. 4b. The detailed I-FFT image corresponding to the marked nanoparticle, and noted with a dashed circle, clearly shows the interatomic distances of 2.65 and 4.70 Å (Fig. 4c).

As a representative example from the V doped SnO_2 nanoparticles, a HRTEM image from $Sn_{0.85}V_{0.15}O_2$ is shown in Fig. 4d. The corresponding FFT pattern along the [001] zone axis is included in Fig. 4e, while the detailed I-FFT image from the nanoparticle marked in Fig. 4d shows interatomic distances of 0.48 nm along both perpendicular directions. The unit cell is marked in Fig. 4f.

The compositional studies of these samples, performed by EDS microanalysis in the electron microscope, confirm that

Fig. 2 (a) A low magnification TEM image of the SnO_2 hydrothermal sample, showing the high dispersion in sizes. (b) A HRTEM image with a nanoparticle highlighted. The reticular parameters and unit cell of the rutile structure are indicated. (c) The FFT pattern along the [1$\bar{1}$1] axis.
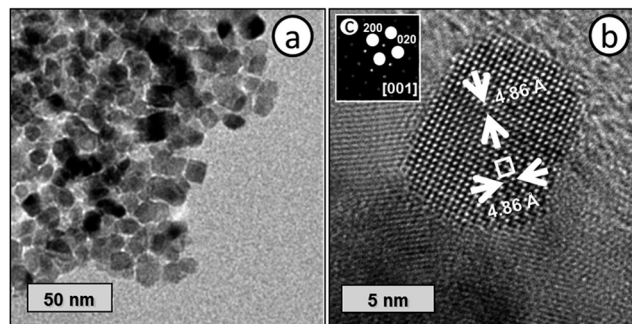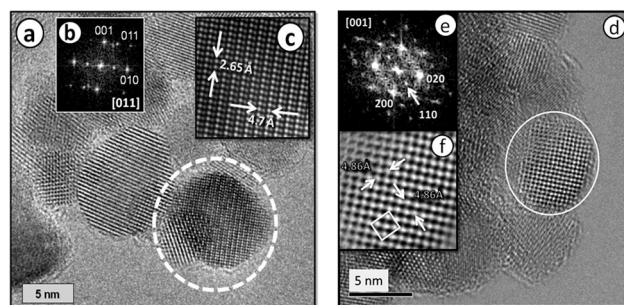

Fig. 4 (a) An HRTEM image of the $Sn_{0.85}Cr_{0.15}O_2$ nanoparticles obtained by the LQM. (b) The FFT pattern along the [011] axis of the rutile structure. (c) The I-FFT image showing the reticular parameters and the unit cell of the rutile [011] plane. (d) The HRTEM image of the $Sn_{0.85}V_{0.15}O_2$ nanoparticles synthesized by the LQM. (e) The FFT pattern along the [001] zone axis. (f) The I-FFT image showing the reticular parameters and the unit cell of the rutile structure.

all of the crystals have a homogeneous cationic composition, which is in good agreement with the nominal composition. Fig. 5 shows the EDS spectra obtained from V, Cr and Mn doped SnO_2 nanoparticles, as an example.

Table 2 summarizes the average cationic compositions for the doped SnO_2 samples with a higher content (15%) of V, Cr and Mn, which demonstrates the high accuracy achieved in the LQM doping process even for cationic compositions as high as 15%, while keeping a high degree of crystallinity.

Cathodoluminescence

The incorporation of transition metal dopants creates intermediate energy states in the band gap of the SnO_2, thus changing the associated radiative-recombination processes in the nanoparticles. Moreover variations in the optical properties due to the reduced size of the nanoparticles and the associated structure of the defects caused by the doping could be promoted. For this reason, the study of the luminescent properties of the doped SnO_2 nanoparticles investigated in this work could lead to gain insights in the comprehension of the phenomena involved in the doping process and the dopant-dependent optical properties of the nanoparticles. The wide band gap of SnO_2 (3.6 eV at 300 K) could provide luminescence within a wide spectral range. In our case near bandgap CL emissions around 3.6 eV were not detected even at a low temperature (80 K), as band-to-band transitions or exciton recombinations are hardly observed in SnO_2 due to the dipole-forbidden nature of the energy band structure of this material. However variations on some other emission characteristics from SnO_2 as a function of the dopant have been analyzed and discussed.

In previous work[32] we have described the CL emission from undoped SnO_2, which mainly consists of three emissions in the visible range, which can be identified as the orange band (1.94 eV), the green band (2.25 eV) and the blue band (2.58 eV). It has been demonstrated that the orange band is associated with oxygen vacancy related defects, which control the conductivity in this material, acting as shallow donor levels. The blue band has been attributed to transitions involving surface states,[21] whereas the origin of the green band is still under discussion, although some works associate this emission to oxygen vacancies with two adjacent oxygen atoms missing. No emissions in the infrared range have been observed for SnO_2.
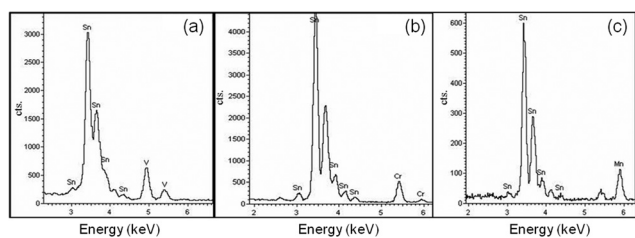
Table 2 The EDS data of the $Sn_{0.85}M_{0.15}O_2$ (M = V, Cr and Mn) samples synthesized by the LQM

	$Sn_{0.85}V_{0.15}O_2$	$Sn_{0.85}Cr_{0.15}O_2$	$Sn_{0.85}Mn_{0.15}O_2$
Sn (% cat.)	86.0 ± 0.4	84.6 ± 0.4	85.3 ± 0.6
M (% cat.)	14.0 ± 0.4	15.4 ± 0.4	14.7 ± 0.6

Initially, undoped SnO_2 nanoparticles synthesized by both the HDT and the LQM have been studied. The representative CL spectra are shown in Fig. 6, where a CL spectrum from commercial bulk SnO_2 is also included for comparison. These spectra have been acquired at 80 K. The intensity of the spectra acquired at 300 K is lower, although they exhibit a similar behavior. The deconvolution of the spectra is also shown in Fig. 6. All of the normalized spectra exhibit an intense orange band (1.94 eV), which dominates in all of the spectra except for the one corresponding to the HDT nanoparticles which is dominated by the green emission (2.25 eV). As both the orange and green bands are associated to oxygen vacancies, their high relative intensity in the CL spectra indicates that these are the predominant defects in the analyzed samples. However, the emission from the LQM and HDT nanoparticles is considerably less intense than that from the bulk SnO_2 due to the decrease in the radiative defects at the nanoscale, or the increase of non-radiative recombination paths. In particular the LQM nanoparticles, the dimensions of which are smaller than those synthesized by the HDT, show the lowest CL intensity. These LQM samples also show a weak emission at 3.2 eV, which is slightly observed in the HDT samples and not observed in the bulk SnO_2. This could be related to transitions involving shallow defect levels, possibly associated with surface-related defects, as the surface-to-volume ratio increases in the nanostructured materials. The HDT nanoparticles present a shoulder at 1.8 eV, which could
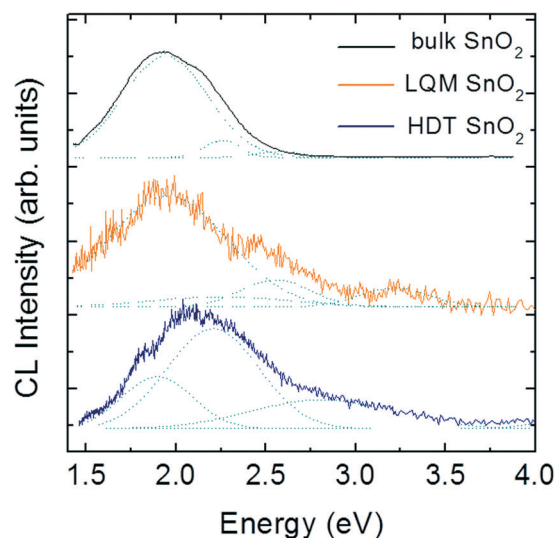

Fig. 5 The EDS spectra of the $Sn_{0.85}V_{0.15}O_2$, $Sn_{0.85}Cr_{0.15}O_2$ and $Sn_{0.85}Mn_{0.15}O_2$ samples obtained by the LQM.

Fig. 6 The CL spectra corresponding to the undoped SnO_2 nanoparticles grown *via* the LQM and the HDT. The CL spectrum from the commercial bulk SnO_2 is shown as a reference.

be due to a variable distribution of defects possibly associated to traps related to singly and doubly ionized oxygen vacancies.[33] The luminescence from the samples grown by the LQM, consisting of SnO_2 nanoparticles doped with Cr, Mn or V in a variable content (5, 10 and 15% cationic fraction), has been investigated.

The CL spectra corresponding to the Cr doped SnO_2 nanoparticles are shown in Fig. 7a. An intense narrow emission centered at 1.79 eV clearly dominates the spectra. Other Cr doped oxides[34–37] also show a strong luminescence at this energy even for low concentrations of Cr^{3+}. The 1.79 eV red luminescence is attributed to Cr^{3+} ions in the SnO_2 lattice, in particular to the radiative transitions involving the ^2E–$^4A_2$ electronic levels, with decay times in the range of milliseconds.[38,39] The high radiative efficiency of this emission makes the nanoparticles optically active at room temperature, as observed in this work. A more detailed analysis of the CL signal confirms the presence of less intense narrow peaks at lower energies, which are attributed to variations in the environment around Cr^{3+}.[40] Increasing the Cr doping enhances the intensity of the main peak at 1.79 eV, as observed in Fig. 7a. In addition to this Cr^{3+} related peak, a less intense emission centered at 2.58 eV, as well as a weak shoulder at 2.25 eV, are observed in the CL spectra. Both emissions can be associated with the blue (2.58 eV) and green (2.25 eV) bands from SnO_2. Usually the orange band (1.94 eV) attributed to oxygen vacancies in the SnO_2 dominates the CL spectra of the undoped SnO_2, nevertheless this emission is quenched in Cr doped SnO_2 nanoparticles. The presence of Cr^{3+} ions in the lattice induces a reduction of the oxygen vacancies related defects responsible from the orange band.

Vanadium doped SnO_2 nanoparticles present a CL emission in the range between 2.1 and 2.5 eV, as observed in Fig. 7b. This green emission presents a complex behavior as it is formed by different narrow components. In particular a narrow emission centered at 2.15 eV, as well as emissions between 2.25 and 2.5 eV, can be distinguished. This green luminescence can be attributed to donor–acceptor transitions involving vanadium-related deep acceptor levels, as reported in similar vanadium doped oxides.[41] The intensity of the emission centered at 2.5 eV decreases as the content of vanadium increases, as observed in Fig. 7b. In addition, the decrease in the intensity of the orange band (1.94 eV) confirms the reduction in the concentration of oxygen vacancies induced by the presence of the vanadium ions. A less intense emission can be also observed centered at 1.68 eV. Furthermore, a weak shoulder can be distinguished for a low V concentration in the high-energy region of the spectra, around 3.6 eV, which should be related to the near band edge transitions. Emissions at 1.68 eV and 3.6 eV, as well as the total CL signals, are drastically reduced as the vanadium content increases, as observed in Fig. 7b.

The CL spectra acquired on the Mn doped SnO_2 nanoparticles are dominated by an emission around 2.0 eV (Fig. 7c) and a weak shoulder appears at 2.25 eV. As referred by different authors,[42] the dopant emission for the Mn-doped nanocrystals has been restricted to the yellow–orange spectral window. The 2.1 eV emission can be attributed to internal Mn^{2+} transitions involving the $^4T_1$–$^6A_1$ electronic states, as observed in other semiconductor hosts.[43,44] Pradhan et al.[42] stated that Mn^{2+} can act as an efficient luminescence center, by means of effective energy paths involving s–p electronic states from the host, which lead to luminescence at room temperature, as observed in this work. Nonetheless, the association of these emissions with the orange band (1.94 eV) and the green band (2.25 eV) in undoped SnO_2 cannot be ruled out. Samples with a low Mn content also show a low intense emission in the high-energy region of the spectra, around 3.4 eV, which could be related to near band edge transitions. In this case, an increase in the Mn dopant concentration also induces a decrease in the total CL intensity, by reducing the native radiative defects from SnO_2, or increasing the number of non-radiative pathways.

As observed in Fig. 7d, the luminescence from doped SnO_2 nanocrystals can span over a wide spectral range from near-IR to UV, as a function of the dopant. Red, green or orange emission can be promoted by doping with Cr, V or Mn respectively, which can be useful in the functionalization of these nanoparticles. Further studies are required to fully understand the mechanism involved in the doping process and the luminescence of these nanoparticles, although these results could serve as a model for other doped semiconductor oxides.

It is worth pointing out that quantum confinement effects were not observed in this luminescence study, which is different from the results reported for other semiconductor nanoparticles.[45,46] Despite the reduced size of the here investigated nanoparticles, the small bulk exciton Bohr radius for SnO_2 (2.75 nm), as well as the low efficient luminescence associated with the band gap transitions in SnO_2, could hinder these effects.
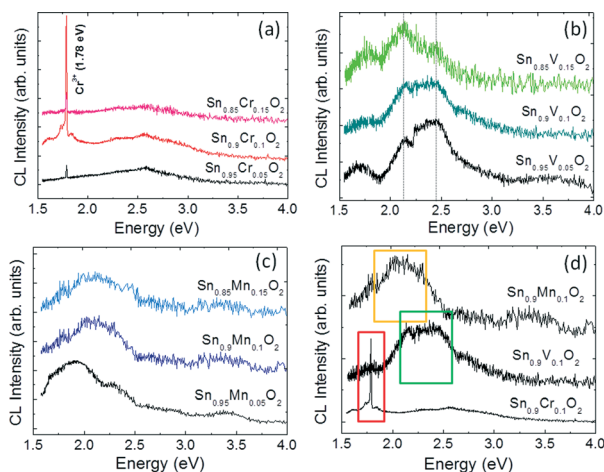

Fig. 7 The CL spectra from the (a) Cr (b) V and (c) Mn doped SnO_2 nanoparticles with a variable dopant concentration grown via the LQM and (d) a comparison between the CL spectra corresponding to the Cr, V and Mn doped SnO_2 nanoparticles with the same dopant concentration: $Sn_{1-x}M_xO_2$ (x = 0.1; M = V, Cr, Mn).

Conclusions

The HDT and LQM have been used to synthesize doped SnO_2 nanoparticles. It has been found that the synthesis of $Sn_{1-x}M_xO_2$ ($x = 0, 0.05, 0.1, 0.15$; M = V, Cr, Mn) nanoparticles using the liquid mix method (LQM) permits the achievement of a high control of both the final particle size and chemical composition. On the other hand, the hydrothermal method (HDT) induces both an agglomeration of the nanoparticles with a high dispersion of sizes and occasionally the segregation of a secondary phase. The doped nanoparticles synthesized via the LQM show an average particle size of around 6 nm, with a rutile-type structure and a high degree of crystallinity. The differences in the chemical kinetics can be due to the variation in the reactivity of the starting compounds in the basic solution under hydrothermal conditions, since this factor has a marked influence on the product dissolution rate, and also, a low chemical reactivity of the hydrothermal solution at temperatures below 180 °C in low concentrated NaOH solutions (0.15 M).

The cathodoluminescence results show that doping the SnO_2 nanoparticles with Cr, V or Mn, induces red, green or orange emissions, respectively. As the presence of these transition metal ions increases in the SnO_2 matrix, the total CL signal is reduced. In particular, the orange band (1.94 eV), associated with the oxygen vacancies in SnO_2 and the conductivity of the samples, decreases upon doping. The 1.79 eV emission observed in the Cr doped samples can be associated with the Cr^{3+} intraionic transitions. The green emission in the V-doped SnO_2 nanoparticles can be associated to the vanadium related deep levels, while the yellow–orange emission characteristic of the Mn doped SnO_2 involves Mn^{2+} transitions.

Acknowledgements

Notes and references

1   C. Kiliç and A. Zunger, *Phys. Rev. Lett.*, 2002, **88**, 095501.
2   D. Maestre, J. Ramírez-Castellanos, P. Hidalgo, A. Cremades, J. M. González-Calbet and J. Piqueras, *Eur. J. Inorg. Chem.*, 2007, **11**, 1544.
3   Y. Zhang, A. Kolmakov, S. Chretien, H. Metiu and M. Moskovits, *Nano Lett.*, 2004, **4**, 403.
4   Q. Zhao, H. Lorenz, S. Turner, O. I. Lebedev, G. Van Tendeloo, C. Rameshan, B. Klötzer, J. Konzett and S. Penner, *Appl. Catal., A*, 2010, **375**, 188.
5   C. Wang and M. Chen, *Mater. Lett.*, 2009, **63**, 389.
6   Z. D. Li, Y. Zhou, T. Yu, J. G. Liu and Z. G. Zou, *CrystEngComm*, 2012, **14**, 6462.
7   W. W. Wang, Y. J. Zhu and L. X. Yang, *Adv. Funct. Mater.*, 2007, **17**, 59.
8   B. Drevillon, S. Kumar, P. Roca i Cabarrocas and J. M. Siefert, *Appl. Phys. Lett.*, 1989, **54**, 2088.
9   C. Lee, B. Nam, W. Choi, J. Lee, D. Choi and Y. Oh, *Mater. Lett.*, 2011, **65**, 722.
10   P. I. Archer, P. V. Radovanovic, S. M. Heald and D. R. Gamelin, *J. Am. Chem. Soc.*, 2005, **127**, 14479.
11   H. Kimura, T. Fukumura, M. Kawasaki, K. Inaba, T. Hasegawa and H. Koinuma, *Appl. Phys. Lett.*, 2002, **80**, 94.
12   M. J. Osiak, E. Armstrong, T. Kennedy, C. M. Sotomayor Torres, K. M. Ryan and C. O'Dwyer, *ACS Appl. Mater. Interfaces*, 2013, **5**, 8195.
13   D. H. Wang, R. Kou, D. Choi, Z. G. Yang, Z. M. Nie, J. Li, L. V. Saraf, D. H. Hu, J. G. Zhang, G. L. Graff, J. Liu, M. A. Pope and I. A. Aksay, *ACS Nano*, 2010, **4**, 1587.
14   P. D. Borges, L. M. R. Scolfaro, H. W. L. Alves, E. F. Da Silva and L. V. C. Assali, *Nanoscale Res. Lett.*, 2011, **6**, 146.
15   T. Yanagimoto, Y.-T. Yu and K. Kaneko, *Sens. Actuators, B*, 2012, **166–167**, 31.
16   M. Shoyama and N. Hashimoto, *Sens. Actuators, B*, 2003, **93**, 585.
17   R. S. Ningthoujam, V. Lahiri Debdutta Sudarsan, H. K. Poswal, S. K. Kulshreshtha, S. M. Sharma, B. Bhushan and M. D. Sastry, *Mater. Res. Bull.*, 2007, **42**, 1293.
18   Y. Zuo, S. Ge, L. Zhang, S. Yan, X. Zhou and Y. Xiao, *J. Alloys Compd.*, 2009, **475**, 60.
19   S. Sambasivam, B. C. Choi and J. G. Lin, *J. Solid State Chem.*, 2011, **184**, 199.
20   C. Van Komen, A. Thurber, K. M. Reddy, J. Hays and A. Punnoose, *J. Appl. Phys.*, 2008, **103**, 07D141.
21   A. Kar, S. Kundu and A. Patra, *J. Phys. Chem. C*, 2011, **115**, 118.
22   N. Dave, B. G. Pautler, S. S. Farvid and P. V. Radovanovic, *Nanotechnology*, 2010, **21**, 134023.
23   S. Ghosh, D. De Munshi and K. Mandal, *J. Appl. Phys.*, 2010, **107**, 123919.
24   R. Alexandrescu, I. Morjan, F. Dumitrache, R. Birjega, C. Fleaca, I. Soare, L. Gavrila, C. Luculescu, G. Prodan, V. Kuncser and G. Filoti, *Appl. Surf. Sci.*, 2011, **257**, 5460.
25   M. Hirano, H. Dozono and T. Kono, *Mater. Res. Bull.*, 2011, **46**, 1384.
26   M. P. Pechini, 1967, *U.S. Patent* no. 3330697.
27   S. D. Shannon, *Acta Crystallogr., Sect. A: Cryst. Phys., Diffr., Theor. Gen. Crystallogr.*, 1976, **32**, 751.
28   J. Hays, A. Punnoose, R. Baldner, M. H. Engelhard, J. Peloquin and K. M. Reddy, *Phys. Rev. B: Condens. Matter Mater. Phys.*, 2005, **72**, 075203.
29   K. Sato, Y. Yokoyama, J.-C. Valmalette, K. Kuruma, H. Abe and T. Takarada, *Cryst. Growth Des.*, 2013, **13**, 1685.
30   E. R. Leite, T. R. Giraldi, F. M. Pontes, E. Longo, A. Beltrán and J. Andrés, *Appl. Phys. Lett.*, 2003, **83**, 1566.
31   S. Das, S. Kar and S. Chaudhuri, *J. Appl. Phys.*, 2006, **99**, 114303.
32   D. Maestre, A. Cremades and J. Piqueras, *J. Appl. Phys.*, 2005, **97**, 044316.
33   A. Kar, M. A. Stroscio, M. Dutta, J. Kumari and M. Meyyappan, *Semicond. Sci. Technol.*, 2010, **25**, 024012.

34 G. C. Vásquez, M. A. Peche-Herrero, D. Maestre, A. Cremades, J. Ramírez-Castellanos, J. M. González-Calbet and J. Piqueras, *CrystEngComm*, 2013, **15**, 5490.

35 S. Fujihara and Y. Shibata, *J. Lumin.*, 2006, **121**, 470.

36 I. López, E. Nogales, B. Méndez, J. Piqueras, A. Peche, J. Ramírez-Castellanos and J. M. González-Calbet, *J. Phys. Chem. C*, 2013, **117**, 3036.

37 P. Gluchowski and W. Strek, *Mater. Chem. Phys.*, 2013, **140**, 222.

38 E. Nogales, J. A. García, B. Méndez and J. Piqueras, *J. Appl. Phys.*, 2007, **101**, 033517.

39 S. Wang, M.-W. Shao, G. Shao, H. Wang and L. Cheng, *Chem. Phys. Lett.*, 2008, **460**, 200.

40 I. S. Altman, P. V. Pikhitsa, M. Choi, J. I. Jeong, H.-J. Song, I. E. Agranovski and T. E. Bostrom, *Appl. Phys. Lett.*, 2003, **83**, 3689.

41 S. Müller, M. Lorenz, C. Czekalla, G. Benndorf, H. Hochmuth, M. Grundmann, H. Schmidt and C. Ronning, *J. Appl. Phys.*, 2008, **104**, 123504.

42 N. Pradhan, D. M. Battaglia, Y. Liu and X. Peng, *Nano Lett.*, 2007, 7, 312.

43 I. S. Altman, P. V. Pikhitsa, M. Choi, H.-J. Song, A.G. Nasibulin and E. I. Kauppinen, *Phys. Rev. B: Condens. Matter*, 2003, **68**, 125324.

44 D. J. Norris, N. Yao, F. T. Charnock and T. A. Kennedy, *Nano Lett.*, 2001, **1**, 3.

45 S. S. Walavalkar, C. E. Hofmann, A. P. Homyk, M. D. Henry, H. A. Atwater and A. Scherer, *Nano Lett.*, 2010, **10**, 4423.

46 F. Gu, S. F. Wang, C. F. Song, M. K. Lü, Y. X. Qi, G. J. Zhou, D. Xu and D. R. Yuan, *Chem. Phys. Lett.*, 2003, **372**, 451.